A Nanostructure-Based High-Temperature Selective Absorber-Emitter Pair for a Solar Thermophotovoltaic System with Narrowband Thermal Emission

Zhipeng Hu[1], Yuan Zhang[1, *], Liu Liu[1], Liu Yang[2], and Sailing He[1, 2]

Abstract—Using absorber-emitter modules, solar thermophotovoltaic (STPV) systems could potentially break through the Shockley-Queisser limit. Efficient spectral selectivity and high temperature endurance are the keys to this technology. In this paper, a high-efficiency selective absorber-emitter module based on refractory material nanostructures is designed for solar thermophotovoltaic applications. Our numerical simulations show that the proposed absorber-emitter module could provide a specified narrowband emission spectrum above the bandgap with optimal bandwidth, and its performance is robust and independent of incident angle and polarization. According to detailed balance calculations, over a broad range of module temperatures, the solar cell efficiency of our design could surpass the Shockley-Queisser limit by 41%.

1. INTRODUCTION

The reduction of fossil fuel supplies forces people to find new alternative energy sources. Solar energy, as an emerging renewable energy source, has received increasing attention: converting solar energy into electricity is becoming a common method to use solar power. In particular, solar photovoltaic technology is considered one of the most promising technologies and is now widely used around the world. By 2020, it is expected that the cumulative installed capacity of the global PV system could be between 490 and 716 GW, but in the energy structure ratio it is still less than 1%. In addition to high construction costs, there is a fundamental reason for the low efficiency of solar energy conversion.

The primary factor limiting the conversion efficiency of a solar cell is the Shockley-Queisser efficiency limit (SQ limit), which contains two main intrinsic loss mechanisms: sub-bandgap radiation loss, in which sub-bandgap photons cannot be absorbed to excite electron-hole pairs, and the thermalization loss resulting from emission above the bandgap causing electrons to have extra irregular thermodynamic movement. Theoretically, at room temperature, the maximum efficiency of an ideal single junction cell is no higher than 41% at maximum concentration, and it will likely fall to 25% for lower concentrations [1].

In order to further improve the utilization of solar power, a large number of studies have been carried out. One idea is to fabricate multi-junction PV cells with multiple semiconductor materials to match the solar spectrum, broadening the effective spectral width by splicing multiple bandgap materials. With adequate fusion bands, the utilization efficiency of solar energy, in theory, can reach a limit of 86.8% [2]. However, this technology is not yet mature, and it is complex and costly and only 43% efficiency has been achieved in the laboratory [3]. Another solution is to transfer the sun's rays into selective thermal radiation with intermediate structures and emit them towards a solar cell directly above the bandgap, known as solar thermophotovoltaics (STPV) [4–13]. To a single junction cell, the

theoretical efficiencies of this device have been shown up to 54% for non-concentrations and 85% for full concentration [12].

As shown in Fig. 1, the intermediate structure consisting of an absorber-emitter pair, which is the key component for the solar thermal photovoltaic technology, is specifically designed to have spectral selectivity: the absorber's absorption spectrum should cover the entire solar spectrum, while the long-wavelength radiation should also be suppressed to reduce the system's radiation loss; the emitter's radiation spectrum should be higher (but could not be too much higher) than the bandgap wavelength (to avoid extra thermalization loss). Such design could efficiently avoid the intrinsic loss mechanisms of SQ limit, and finally, the useful energy gets to the PV cell could reach a very high proportion.
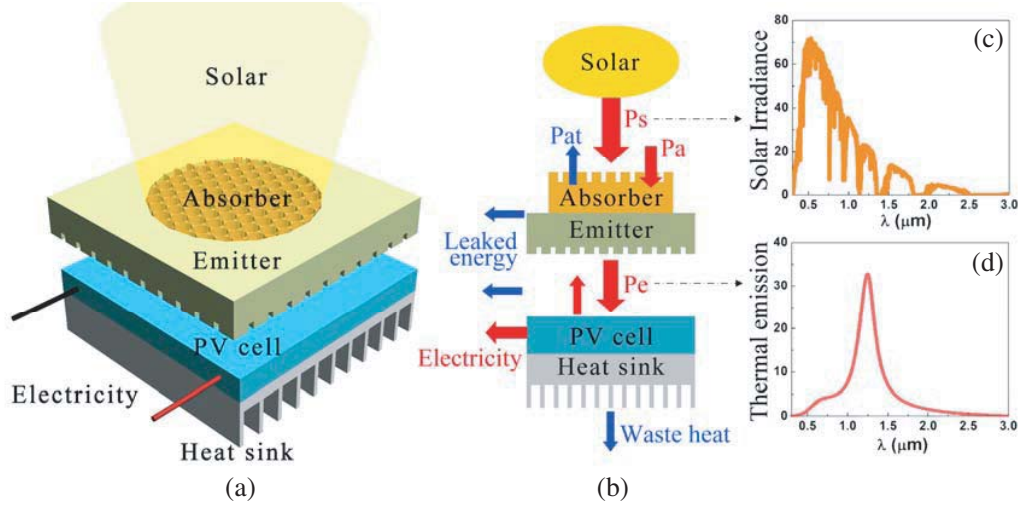
Figure 1. (a) Schematic of a planar STPV consisting of absorber-emitter module. (b) Energy flux diagram of the STPV that converts solar radiation with a broadband spectrum (c) into a narrowband spectrum matched to (d) the PV cell.

Besides the designed excellent spectral selectivity, another essential point is that the intermediate structure should withstand high temperatures, as its performance is limited by the melting points of the construction materials. Therefore, refractory materials are preferred, such as tungsten (W) and tantalum (Ta), whose melting points are not less than 3000 K. At present, many studies have been based on tungsten or tantalum to design the absorber and emitter devices [14–25], but the general efficiency is still not high enough. Furthermore, some of the designs use low-melting point dielectric materials to improve the system's performance [21–25], which will apparently limit the application of STPV devices. Therefore, the STPV system still has much to be improved in some respects.

In this paper, we design an absorber-emitter module based on refractory material for a $\lambda_{PV} = 1.53\,\mu\text{m}$ solar cell to overcome the weaknesses mentioned above. The proposed absorber is composed of W triangles in a hexagonal close-packed array on a W substrate, which can effectively capture solar light of wavelength less than $2\,\mu\text{m}$. This feature gives full play to the intrinsic absorption of tungsten material, makes the broadband absorption spectrum close to 100%, and covers almost the entire solar spectrum (AM1.5). The proposed emitter is composed of Ta nano-squares in square array on a Ta substrate. The intrinsic absorption of Tantalum is weaker than tungsten, and it is suitable for the design of a narrow-band emitter. Our optimized emitter can emit light with optimal bandwidth, which keeps the PV cell from producing extra thermalization loss. We have also calculated their electric field distributions at special frequency points to show the inner mechanisms. The sensitivity to the polarizations and incident angles has also been studied, and it is found that their performances are fairly stable. All of the quantitative full-field electromagnetic simulations were conducted with the finite-difference time domain (FDTD) method by using the commercial software of Lumerical FDTD Solutions.

Finally, we have calculated the solar cell efficiency of our design based on SQ analysis [1]. In the efficiency calculation, we introduce the impedance matching factor and the ratio of open-circuit voltage and band-gap voltage so that the calculation results are more realistic. It is calculated that the solar cell efficiency can be up to 51% with increased operating temperature, while taking into account the relationship between the sun focus and the structure's working temperature the efficiency will be reduced slightly, to about 45%. The solar energy efficiency of our design will break through the traditional efficiency limits for solar cells (41%) over a broad range of solar concentrations.

2. ABSORBER DESIGN

In solar thermophotovoltaic systems, the absorber is responsible for absorbing the incident light and determines the system's total input energy. Therefore, the absorber's capacity for sunlight absorption must be strong enough, which requires that the absorption range can cover the entire solar spectrum, such as AM1.5 from $0.3\,\mu m$ to $2.5\,\mu m$. Absorbing solar energy as far as possible across the spectrum can increase the thermal equilibrium temperature of the absorber-emitter module so that the emitter can output a higher quality photon energy. At the same time, the heat radiation loss of the absorber itself should be prevented in order to ensure a sufficiently high thermal equilibrium temperature. According to Kirchhoff's law, an object emits as much radiation as it absorbs in thermal equilibrium, therefore the absorptivity of the absorber in longer wavelengths should be weaker. These requirements indicate that an ideal solar energy absorber should have zero absorption outside the cut-off wavelength and complete absorption within the cut-off wavelength. However, in actual design, the absorption outside the cut-off wavelength cannot be exactly zero, so the selection of the absorber's cut-off wavelength must give consideration to both the absorption and energy loss. In addition, the absorber design should also use high-temperature materials in fabrication, as the operating temperature is usually higher than $1500\,K$. At present, many studies have been done on spectral selective absorbers based on tungsten and tantalum, such as microporous structures [18–20] and pyramid structures [16, 21, 22], but their absorption efficiency is still not outstanding enough; these structures often require a much higher aspect ratio. For example, the structure in Ref. [20] requires a pore diameter of $1.45\,\mu m$ and a hole depth of $8\,\mu m$, which is difficult to realistically produce.

At the same time, it should also be noted that in the thermal photovoltaic solar cell system, the absorber usually works with a focusing lens to allow adequate light energy to be collected. With increased focusing, the amount of light with large incident angles will also increase, so the design of the absorber should consider its dependence on the incident angle and polarization. In the case of large-angle incidence, the particle structure can be applied to the structural design to ensure that the area of interaction between the structure and light cannot be reduced, such as spherical particles [25] and pyramidal structures [16]. High refractive index dielectric filling can also be used to improve the performance of microporous structures with poor oblique incidence properties, making it possible for light incident at large angles to enter the interior of the structure by the refraction of light [24]. However, this approach leads to a decrease in the structural tolerance in temperature, as the melting point of the dielectric is not high enough.

Combining the advantages of microporous structures and granular structures discussed above, we propose a curved triangular array structure made of metal tungsten such that the absorber can maintain high light absorption at different angles and polarizations. Our design, as shown in Fig. 2(a), is composed of a hexagonal close-packed array of cavities with diameter $D = 1\,\mu m$, gap distance between each triangle $g = 100\,nm$, and depth $h = 1\,\mu m$. This kind of structure has a shallow cavity, and its aspect ratio is 1, which makes it easy to manufacture and suitable for mass production. For example, inexpensive colloidal sphere template etching technology can be used to make it.

For the simulation, a plane wave propagates along the z direction with the electric and magnetic fields polarized along the x and y directions, respectively. Periodic boundaries are set along the x and y directions, while perfectly-matched layers are added in the z direction. The dielectric constant of tungsten is taken from Ref. [26].

For normally incident light with x-polarization ($\theta = \varphi = 0$, i.e., electric field parallel to the x-axis), the absorption spectra of W absorber (red line) and bare W slab (blue line) are calculated respectively, as shown in Fig. 2(b). From the spectrum, we can see such an absorber nearly acts as
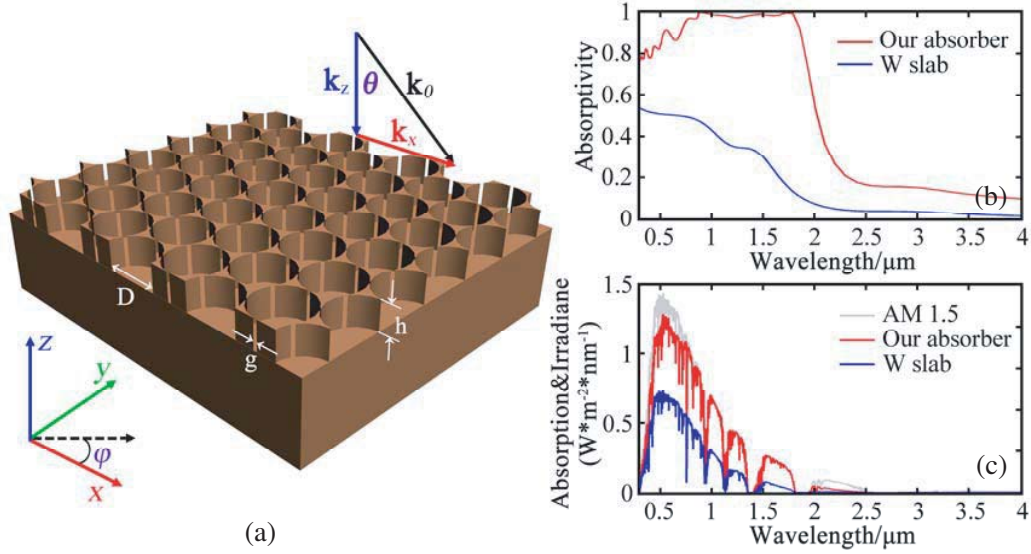
Figure 2. (a) Schematic of a selective absorber consisting of a hexagonal close-packed array of cavities with diameter D, gap g, and depth h; and the incident light has free-space wave vector k_0, incident angle θ, and azimuthal angle φ. (b) Simulated absorption spectra for W absorber and bare W slab with normally-incident light of x-polarization ($\theta = \varphi = 0$, i.e., electric field parallel to the x-axis). (c) The AM1.5 solar irradiance spectrum and the products of the absorptivity with it.

a blackbody at $\lambda < 2\,\mu$m, while its absorptivity is decreased dramatically at longer wavelengths of $\lambda > 2\,\mu$m. These absorption characteristics not only allow the absorber to efficiently absorb sunlight, but also suppress the absorber's radiation at the wavelength range longer than $2\,\mu$m, which lends itself to excellent solar energy storage capabilities. At $\lambda < 2\,\mu$m, compared to the pure semi-infinite tungsten slab, the absorptivity is increased from less than 50% to close 100%, as the hexagonal close-packed structure provides an impedance matching mechanism between free space and tungsten. In Fig. 2(c), the products of the absorptivity with AM1.5 spectra radiance (gray line) are depicted. As can be seen, the absorber efficiency is above 90% for the AM1.5 spectrum.

In order to further investigate the functional mechanisms of hexagonal close-packed structures in optical absorption, we chose four characteristic absorption peaks to calculate their electric field distributions. As shown in Fig. 3, we have calculated the electric field distributions of four absorption points (520 nm, 700 nm, 965 nm, and 1770 nm), including a cross-sectional (xy plane) and overhead view (xz plane).

The top row in Fig. 3 shows that the field intensity is increasing with the wavelength, and for the bottom row, we can see that there are 4, 3, and 2 hot spots (different standing wave modes) in the gap between the adjacent triangle particles when the incident light has wavelength $\lambda = 520$ nm, $\lambda = 700$ nm, and $\lambda = 965$ nm, respectively. Here, a simple approximate equation can be used to depict the relationship between the number (m) of the hot spots, the wavelength (λ) of the incident light, and the height (h) of the triangle particles: $m\lambda = 2h$. This expression is valid without involving any other parameters of the tungsten nanostructure which means that the triangle particles do not affect the forming of the standing waves, which are mainly caused by the metal gaps. By searching the dispersion relation of tungsten [26], we can find that the optical properties of tungsten behave more like a dielectric, as the real parts of its permittivity are positive within 1 um, therefore no surface plasmons are excited when the light ($\lambda < 1\,\mu$m) propagates from the air to the air/tungsten interface. Fortunately, the imaginary parts of tungsten's permittivity are relatively large, so although no surface plasmons exist, our design still has excellent light absorption abilities by increasing the contact area with the nanostructure, as shown in Fig. 2(b). Conversely, when $\lambda > 1\,\mu$m, the structure will have the potential to achieve plasmonic oscillation as long as the structural dimensions are proper. In Fig. 3(d2),
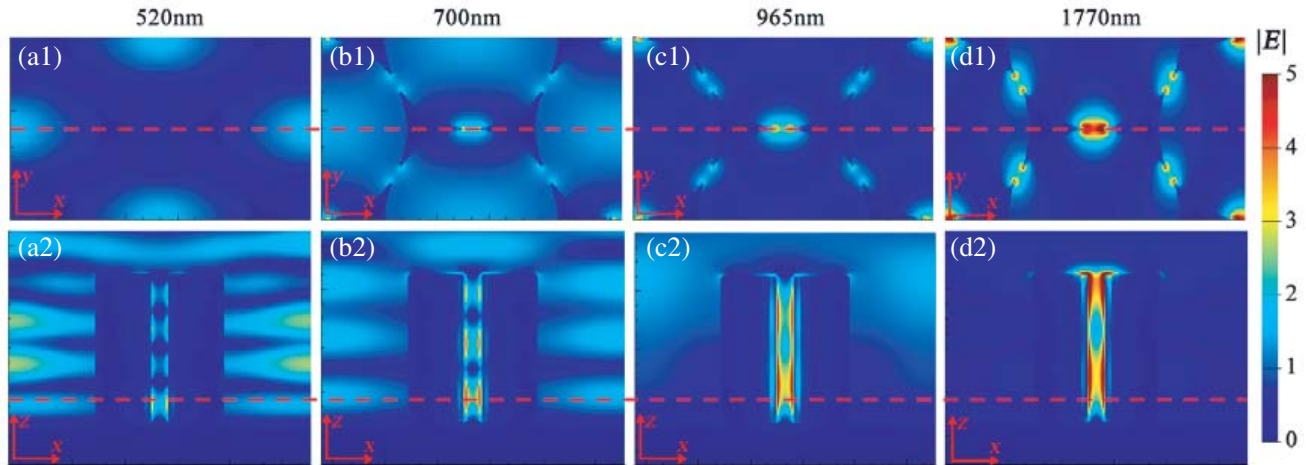
Figure 3. Electric field distributions of the absorber in the xy plane (top row) and the xz plane (bottom row) at (a1), (a2) $\lambda = 520\,\mathrm{nm}$; (b1), (b2) $\lambda = 700\,\mathrm{nm}$; (c1), (c2) $\lambda = 965\,\mathrm{nm}$; and (d1), (d2) $\lambda = 1770\,\mathrm{nm}$. The red dashed lines in the top (bottom) figures indicate the positions of the xz (xy) planes in the bottom (top) figures.

two hot spots similar to those in Fig. 3(c2) can be found in the gap between the nanoparticles, but those in the former are much stronger. There is no doubt that the hot spots in Fig. 3(d2) were created by localized surface plasmon resonance (LSPR), as the resonance wavelength ($1.77\,\mu\mathrm{m}$) is larger than the structural height, and the electric field enhancement is remarkably high. Returning to the absorber's absorption spectrum (Fig. 2(b)), an absorption peak is seen at $\lambda = 1.77\,\mu\mathrm{m}$, and then rapidly falls as the wavelength increases because the effect of LSPR is particularly sensitive to the structural dimensions; for longer wavelength light, the structure is too small and slab-like, so no other resonance peak arises and no light is confined.

The spectral absorber is usually used in conjunction with a focusing lens to absorb as much incident energy as possible, so the absorber should maintain an efficient, spectrally selective absorption at all incidence angles. In other words, the cutoff wavelength should be stabilized at a fixed wavelength (In our design, the cut-off wavelength selected is $2\,\mu\mathrm{m}$) without excessive bias when the incident angle changes, ensuring that the incident light can be absorbed completely. To confirm this, we have calculated the absorption spectra of our structure at different incident angles and polarizations. Because of the rotational symmetry of the hexagonal close-packed structure, the structure is repeated every $60°$. Therefore, we only calculated two cases, with incident azimuth angle φ of $0°$ and $90°$. These two cases correspond to the horizontal component of the electric field parallel and perpendicular to the triangle symmetry axis, respectively (as the coordinates shown in Fig. 1).

As shown in Fig. 4, the absorption spectrum of the structure varies with the angle of incidence (from $0°$ to $60°$) under the irradiation of p-polarized and s-polarized light. The absorption spectrum of p-polarized light broadens as the incident angle increases, while the s-polarized case has shown the opposite tendency. As the s-polarized light has a shortcoming in the excitation of plasma resonance, the absorption capacity decreases slightly relative to the p-polarized case. However, the cut-off wavelength can be located at the position about $2\,\mu\mathrm{m}$ without significant fluctuation, which indicates that the structure is insensitive to change of the incident angle and polarization and can maintain the selective absorption ability when the focusing lens is used. The incident angle insensitivity and polarization independence are achieved because the absorption of the structure mainly depends on the coupling between the adjacent triangle particles, as discussed previously. The gap between the particles is constant, which leads to a fixed corresponding resonance wavelength, and then the spectrum is stable enough.
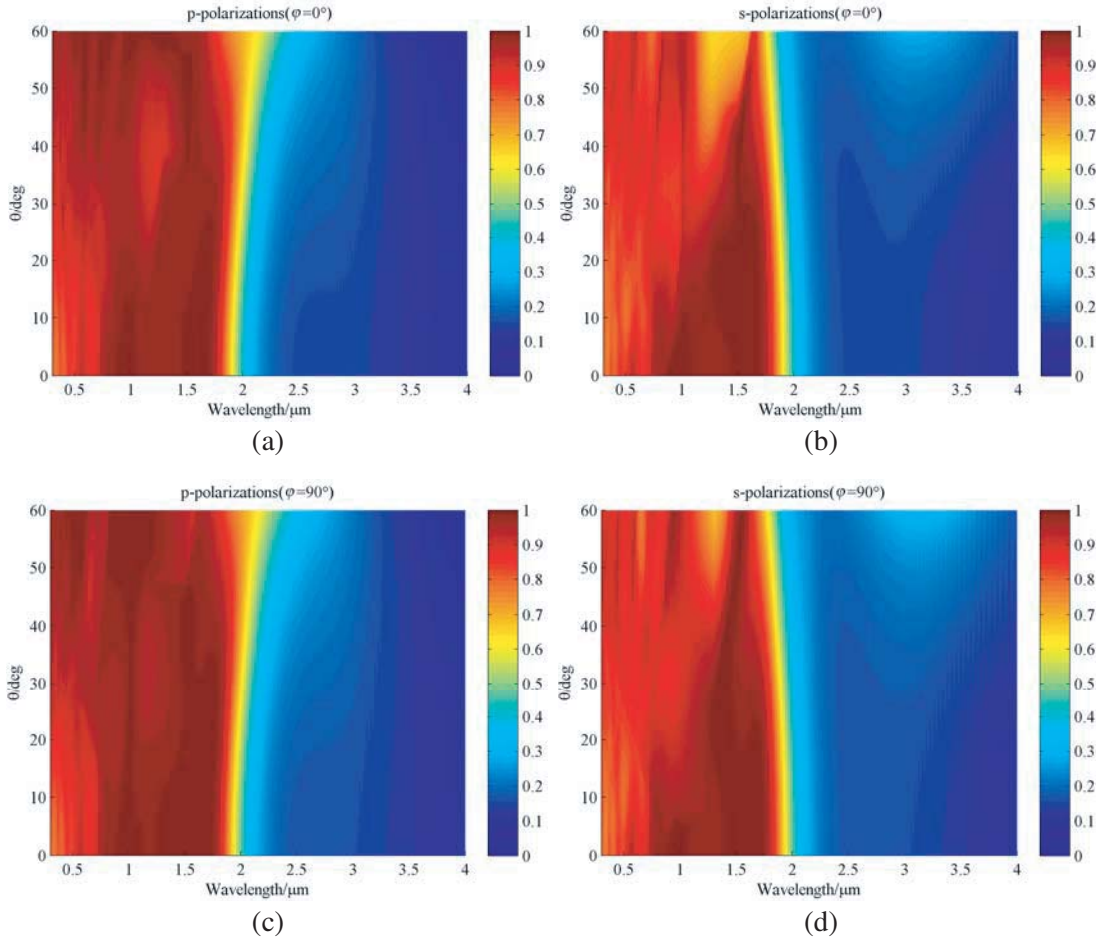
Figure 4. Absorptivity spectrum of the proposed W absorber with (a) *P*-polarized light and (b) *S*-polarized light as a function of incident angle θ at $\varphi = 0°$, with (c) *P*-polarized light and (d) *S*-polarized light as a function of incident angle θ at $\varphi = 90°$.

3. EMITTER DESIGN

Intuitively, an ideal emitter should provide a sharp cut-off of emitter emissivity at the solar-cell band-gap energy to avoid the thermalization loss that results from the electrons' extra irregular thermodynamic movement while completely suppressing sub-band-gap radiation. So far, most emitters are designed with broadband emission [17–20], which have a sharp cut-off of emissivity at the energy of the junction band-gap and do not limit the radiation of higher energy.

However, according to [5] and [21], the detailed balance limit of solar cell efficiency has a peak at a bandwidth of ~ 0.07 [eV]. Since the charge carrier density is directly proportional to the total flux of above-band-gap photons that the emitter radiates, reducing the emitter bandwidth reduces the open circuit voltage and the impedance matching factor, while increasing the emitter bandwidth reduces the ultimate efficiency. Here, we adopt the emitter design concept as outlined in Refs. [5] and [21].

In order to achieve narrow band radiation, both shortwave radiation and longwave radiation should be suppressed effectively. Tantalum, a high melting point material, is chosen to manufacture the emitter because of its low emissivity at long wavelengths and its ability to withstand high temperature environments. The basic idea of our selective emitter design is to fabricate nanocavity geometries on the surface of the tantalum plate and take advantage of the localized surface plasmonic effect to trap the light with a specified resonant frequency to create the narrow-band selective emitter. It should be noted that, according to Kirchhoff's law, an object emits as much radiation as it absorbs in thermal

equilibrium, therefore it is reasonable we study the emitter's radiation spectrum from calculating its optical absorption. For the following discussion, the emissivity spectra of our selective emitter will be calculated indirectly by obtaining its absorptivity spectra, and the emission mechanism will also be discussed from its ability of trapping light.

The geometry of our selective emitter, which is made of Ta nano-squares in square array on Ta substrate, is schematically shown in Fig. 5, where a, h and p represent the side length, the height of each square, and the period of the square array, respectively.
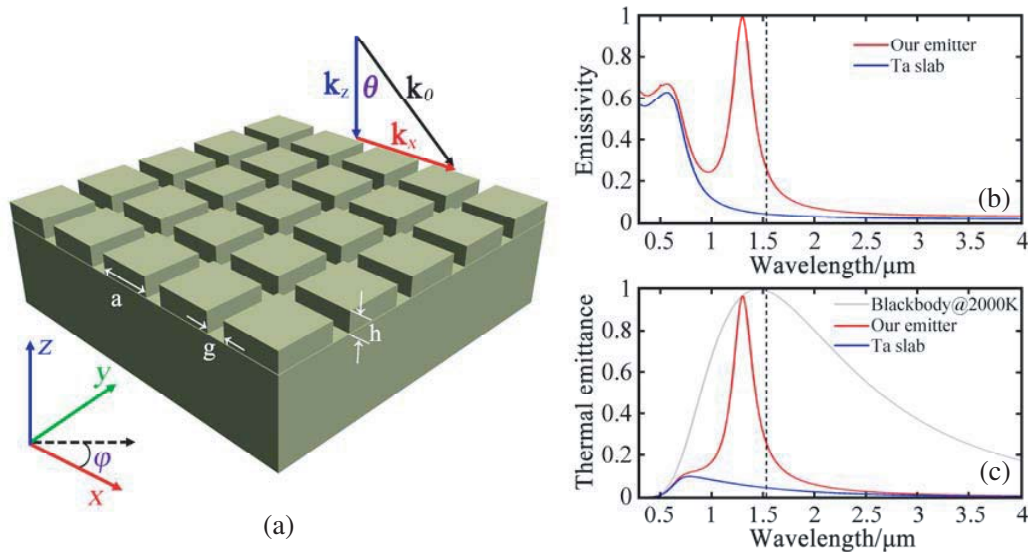
Figure 5. (a) Schematic of slective emitter for free-space wave vector k_0, incident angle θ, and azimuthal angle φ side length a, height h, and period p; (b) Simulated normal emittance for 2D Ta square array (red curve) and the bare Ta slab (blue curve); (c) normalized thermal emittance of our selective emitter (red curve), the bare Ta slab (blue curve), and the blackbody (gray curve) at 2000 K.

The red curve in Fig. 5(b) shows the simulated normal emission spectrum of the structure, with geometric parameters $a = 470$ nm, $h = 140$ nm, and $p = 500$ nm, and the permittivity of Ta taken from Ref. [26]. The simulation settings (incident source and boundary conditions) are the same as used in absorber design. A sharp emittance peak appears in the vicinity of 1.25 μm, and the bandgap of the back PV cells we choose here is $\lambda_{PV} = 1.53$ μm, as the black dash line indicates in Fig. 5(b). There is another peak close to 0.5 μm, as shown on the blue curve in Fig. 5(b), which is the intrinsic emission of Ta verified by the calculated emittance of a bare Ta slab (blue curve).

In our design, besides the longer wavelengths (below the bandgap) radiation that should be suppressed, the shorter wavelength region (above the bandgap) should also be suppressed to reduce the heat effect, which means the first emission peak in Fig. 5(b) is an obstacle for the above purpose. Fortunately however, the short-wavelength radiation is always weak when we normalize the emittance spectra to the blackbody radiation at a certain temperature (e.g., 2000 K, as seen in Fig. 5(c)). The normalized emittance spectra of our selective emitter (red curve) is the product of the emissivity and the spectral emittance of an ideal blackbody, and we can see that the first radiation peak of the emitter in short wavelength is almost gone. In addition, the suppression of long-wavelength thermal radiation of our design, which has a sharp cut-off for wavelength longer than 1.53 μm (see Fig. 5(c)), is remarkable.

In order to further investigate the radiation mechanism of the emitter, we have calculated the cross sectional electric field distributions of these two characteristic peaks ($\lambda = 560$ nm and $\lambda = 1300$ nm), as shown in Fig. 6. As mentioned previously, the first radiation peak of the emitter originates from the flat tantalum, which fails to excite a localized surface plasmon mode. Approximately 70% of the incident electromagnetic field is converted into surface plasmon waves and propagates along the metal plane, so in Fig. 6(a) no bound field exists. But in Fig. 6(b), which corresponds to the second radiation peak,
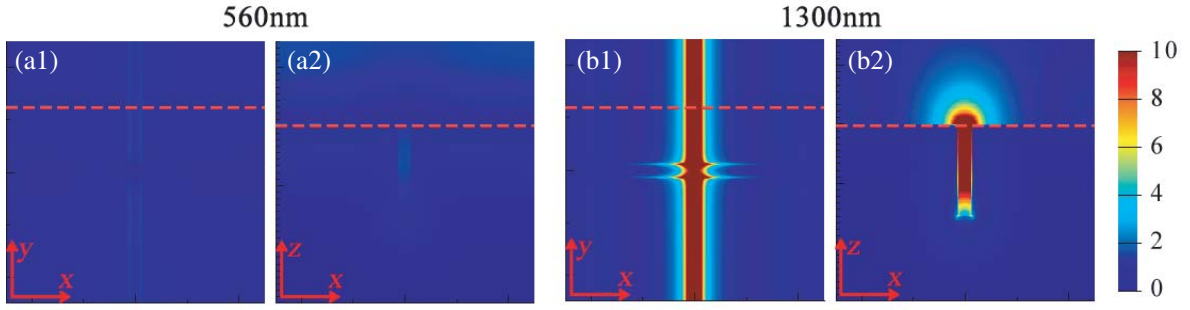
Figure 6. Electric field distributions of the emitter in the xy planes and xz planes at emission peak wavelengths, (a1), (a2) $\lambda = 560\,\mathrm{nm}$ and (b1), (b2) $1300\,\mathrm{nm}$. The red dashed lines in (a1) ((b1)) indicate the positions of the xz (xy) planes in (a2) ((b2)) figures.
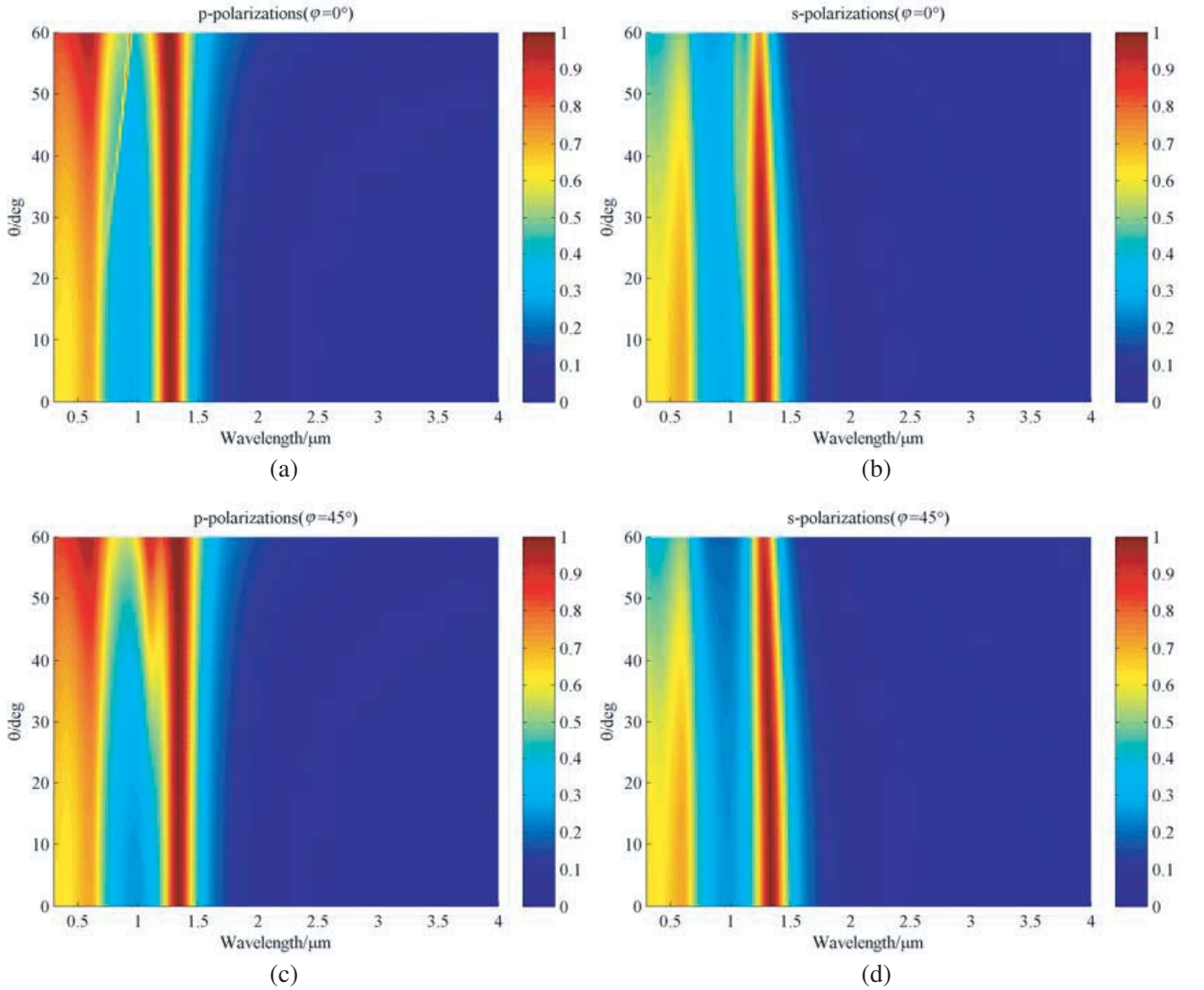
Figure 7. Emissivity spectrum of the proposed Ta emitter with (a) P-polarized light and (b) S-polarized light as a function of incident angle θ at $\varphi = 0°$, with (c) P-polarized light and (d) S-polarized light as a function of incident angle θ at $\varphi = 45°$.

we can see a bright electric hotspot at the gap between each square. That is because the gap acts as a resonant cavity: when the frequency of the incident light matches the cavity resonant frequency, the electromagnetic energy is collected and enhanced through electron oscillation. As a result, a significant localized surface plasmon resonant mode is generated, and the optical field is confined tightly by the gap. Due to the intensely powerful photoelectric coupling effect, the light energy is absorbed completely at the center frequency, which indicates 100% radiation, as shown in Fig. 5(b). By analyzing the electric field distributions of the two radiation peaks, it is shown again that their generation mechanism is different: the former is more related to Ta's intrinsic loss, and the latter is the result of local surface plasmon resonance.

A qualified selective emitter should ensure that the emissivity peak is located in the wavelength range $\lambda < \lambda_{PV}$ and should be stable when to the emitting angle is varying, which can make the radiation component of STPV function in the absence of a focusing lens and make the whole system more compact. Due to the symmetry of the emitter, we only show the results of two azimuthal angles ($\varphi = 0°$ and $\varphi = 45°$), and for each azimuthal angle we calculate the spectrum under different polarizations (i.e., p- and s-polarization) for various incident angles from $0°$ to $60°$. The simulation results are shown in Figs. 7(a)–(d) for different cases. It can be found that the emissivity peaks (warm color) are consistently located at wavelengths around $1.25\,\mu m$ and have great ability for long wave radiation suppression (deep blue) for all cases. For Figs. 7(a) and (c), the emissivity peaks broaden as the incident angle is increased because the coupling effect between the light and the structure primarily relies on the electric field. That is, when incident direction of p-polarizations slopes gradually, the vertical component of the electric field will be increased accordingly, and hence the spectrum peak is broadened. From these figures, it is seen that our emitter shows an efficiently selective radiation, independent of incident angle and polarization. Therefore, the emitter could work in a relatively stable and predictable way either with a focusing lens or not.

4. SYSTEM EFFICIENCY

If the leaked thermal radiation is ignored, the STPV system energy flux through the intermediate module mainly contains four parts: incident sunlight by concentrator (P_s), absorbed energy by absorber (P_a), and thermal emission by absorber (P_{at}) and emitter (P_e), as shown in Fig. 1(b). Their expressions can be written as:

$$P_s\left(N_s\right) = A_a \int_0^{2\pi} d\phi \int_0^{\theta_C} d\theta \sin\left(\theta\right) \cos\left(\theta\right) \int_0^{\infty} dE I_s\left(E\right) \tag{1}$$

$$P_a\left(N_s\right) = A_a \int_0^{2\pi} d\phi \int_0^{\theta_C} d\theta \sin\left(\theta\right) \cos\left(\theta\right) \int_0^{\infty} dE \varepsilon_a\left(E, \theta, \phi\right) I_s\left(E\right) \tag{2}$$

$$P_{at}\left(T\right) = A_a \int_0^{2\pi} d\phi \int_0^{\pi/2} d\theta \sin\left(\theta\right) \cos\left(\theta\right) \int_0^{\infty} dE \varepsilon_a\left(E, \theta, \phi\right) I_{BB}\left(E, T\right) \tag{3}$$

$$P_e\left(T\right) = A_e \int_0^{2\pi} d\phi \int_0^{\pi/2} d\theta \sin\left(\theta\right) \cos\left(\theta\right) \int_0^{\infty} dE \varepsilon_e\left(E, \theta, \phi\right) I_{BB}\left(E, T\right) \tag{4}$$

Here, A_a is the absorber area, and A_e is the emitter area. $\varepsilon_a(E, \theta, \phi)$ is the absorptivity of the absorber, and $\varepsilon_e(E, \theta, \phi)$ is the emissivity of the emitter. $I_s(E)$ is the solar irradiance spectrum, which is assumed to be the AM1.5 solar spectrum for subsequent calculations. $I_{BB}(E, T)$ is the blackbody irradiance spectrum at temperature T. $\theta_c = \sin^{-1}(\sqrt{\frac{N_s \Omega_s}{\pi}})$ is half of the incident cone angle, where N_s is the number of concentrated Suns and $\Omega_s = 68.5\,\mu Sr$ is the solid angle of the Sun as seen from Earth.

The overall system efficiency can be defined as $\eta_{stpv} = \eta_{ae}\eta_{sc}$. The first term is the radiation efficiency of converting sunlight into the thermal emission of emitter by the absorber-emitter pair.

It can be expressed as $\eta_{ae} = P_e/P_s$. According to Equations (1) and (4), we know that the independent variables that determine the value of P_s and P_e are the solar concentrations N_s and equilibrium temperature T, respectively. Therefore, the relationship between these two variables should be clarified first before calculating the radiation efficiency. According to the Law of Conservation of Energy, the incoming and outgoing power should be equal at thermal equilibrium temperature T, thus $P_a(N_s) = P_{at}(T) + P_e(T)$. Based on this formula, we can obtain the equilibrium temperature of the absorber-emitter module under incident solar irradiance with different solar concentrations. As shown in Fig. 8(a), the equilibrium temperature increases with increasing solar concentration, and it will easily go beyond the melting point when the area ratio (A_e/A_a) is small. Then, replacing T with N_s, the radiation efficiency is plotted as a function of solar concentrations with different area ratios (A_e/A_a), as shown in Fig. 8(b). We can see that as the solar concentration increases, the radiation efficiency rises up rapidly and then flattens gradually. According to these two figures, it can be deduced that a larger area ratio can obtain a greater radiation efficiency and the equilibrium temperature would not exceed the
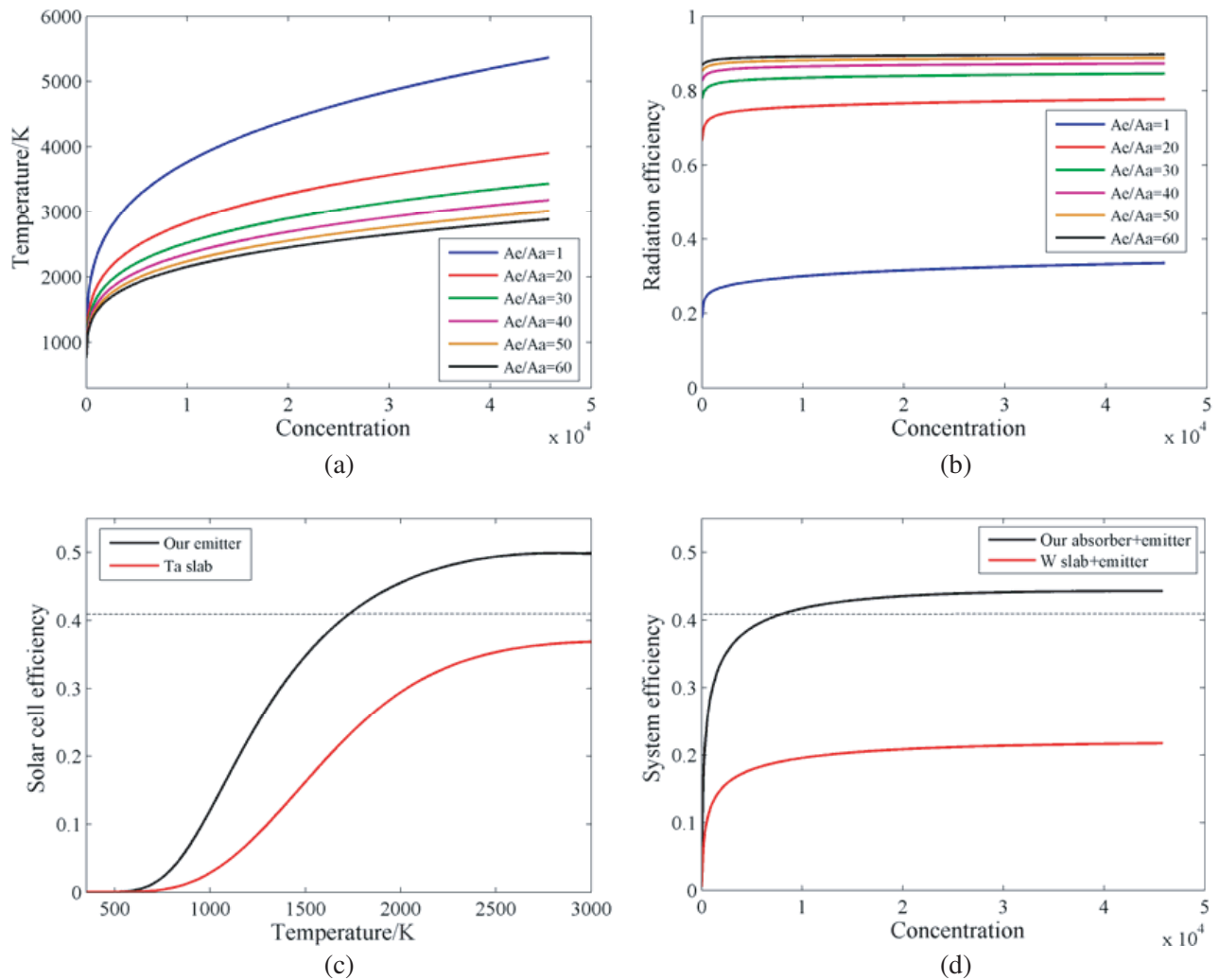
Figure 8. (a) Intermediate equilibrium temperature vs. solar concentration and (b) radiation efficiency vs. solar concentration for the emitter-absorber pair with different area ratios. (c) Solar cell efficiency vs. equilibrium temperature of a 0.81 eV solar cell exposed to radiation from our emitter (black curve) and Ta slab (red curve), gray dashed line indicates the SQ limit at 41%. (d) STPV system efficiency vs. solar concentration for our emitter-absorber pair and W slab-emitter pair with area ratio $A_e/A_a = 50$ (gray dashed line indicates the SQ limit at 41%).

structure's melting point as a result. Therefore, in a practical STPV system, the emitter area should be larger than the absorber area to sustain higher light concentrations and achieve superior intermediate efficiency. In our design, $A_e/A_a = 50$ is an excellent choice, at which radiation efficiency exceeds 90%, and the equilibrium temperature is lower than the structural melting point when the concentration is lower than 4.5×10^4 times, as seen by the black curve shown in Figs. 8(a) and (b). In this calculation, the thermal emission of absorption edge is ignored except for the lit area, as this loss can be avoided in practical design. For example, we can use mirrors to cover the non-concentrated areas for a planar design [12, 23], or bend the emitter to increase the area ratio, such as through folding configurations [12] or a cylindrical geometry [21].

The second term η_{sc} of the system efficiency is the efficiency of generating electrical power from the thermal emission, which is called the solar cell efficiency and controlled by the properties of the emitter and solar cell. It is composed of three parts: $\eta_{sc} = U(T, E_g)\upsilon(T, E_g)m(V_{op})$. $U(T, E_g)$ is the ultimate efficiency and equal to the power contained in excited electron-hole pairs with respect to the incident power. This calculation assumes that one qualified photon ($E \geq E_g$) incident on the solar cell can only excite one electron-hole pair with band-gap voltage $V_g = E_g/q$ (q represents the charge of an electron). The second factor is the ratio between the open-circuit voltage (V_{op}) and the band-gap voltage (V_g), and it contains a non-ideality factor f. The third factor is the impedance matching factor, which is guaranteed to maximize electrical power output from the solar cell under a choice of the operating voltage. The detailed mathematical expression can be found in Ref. [21]. Assuming that the solar cell is at room temperature $T_c = 300$ K, the non-ideality factor $f = 1/2$, and the bandgap wavelength is $\lambda_g = 1.53$ μm (corresponding to the bandgap energy of $E_g = 0.81$ eV), the solar cell efficiency of our structure can be calculated. As shown in Fig. 8(c), the solar cell efficiency is plotted as a function of the emitter's temperature; the dotted line is the SQ limit efficiency of 41%. Clearly, the solar cell efficiency is shown to break though the Shockley-Queisser limit of 41% over a broad range of emitter temperatures, and it reaches a maximum of 51% at 2600 K. As a comparison, the solar cell efficiency of Ta slab (regarded as emitter) is also calculated.

At last, we multiply the radiation efficiency η_{ae} (when $A_e/A_a = 50$) by the solar cell efficiency η_{sc} to obtain the overall system efficiency. The result, as plotted in Fig. 8(d), shows the overall system efficiency as a function of solar concentration. The efficiency is shown to exceed the SQ limit of 41% over a broad range of concentration values (as the black curve shows). As a comparison, we replace our absorber with a W slab and calculate its system efficiency (red curve); obviously, our design has superior performance, as the absorber design is critical and equally as important as the emitter.

The material's constants used in the discussion above are all at room temperature, which would be different from the actual situation as the high temperature environment may affect the optical properties of the materials. This difference should not be ignored as the absorber/emitter's property might be sensitive to the material's constants, especially when the surface plasmon resonance is used in the design. But unfortunately, it is not easy to experimentally measure the permittivity of W or Ta at high temperatures. One compromise method we used here is to restore the material's high temperature permittivity by fitting the experimentally measured emittance of flat materials [27] via the Lorentz-Drude model as described in Ref. [28]. As the measurement error and some uncertainty in data fitting, the simulation precision would be limited, but it can still address some useful points. Based on this scheme, we have calculated the absorption spectrum of the proposed W absorber and Ta emitter at 2400 K, indicated by dashed and gray solid curves in Fig. 9, respectively. It can be seen that the absorptivity (i.e., the emissivity) peak of our emitter drops dramatically and could not be treated as a narrow band emitter anymore. Besides, the absorptivity of both absorber and emitter at long wavelength range rise up significantly, which will cause more radiation loss comparing with those results in previous discussion. Such drawbacks will lower the final system efficiency which is calculated here only 28%. Using the restored optical constants above, we re-optimized two new kinds of emitters (named as New Ta emitter and W emitter) to try to improve the high temperature performance of our STPV system, and the optimized absorption spectrums are also shown in Fig. 9 by blue and red curves, respectively. Two new kinds of emitters are still designed by the same architecture as in Fig. 5, and the optimized geometry parameters are: ($a = 380$ nm, $h = 150$ nm, and $p = 500$ nm) for the New Ta emitter, and ($a = 370$ nm, $h = 160$ nm, and $p = 500$ nm) for the W emitter. Apparently, the curves of New Ta emitter and W emitter are similar, and both could work as a narrow band emitter. The
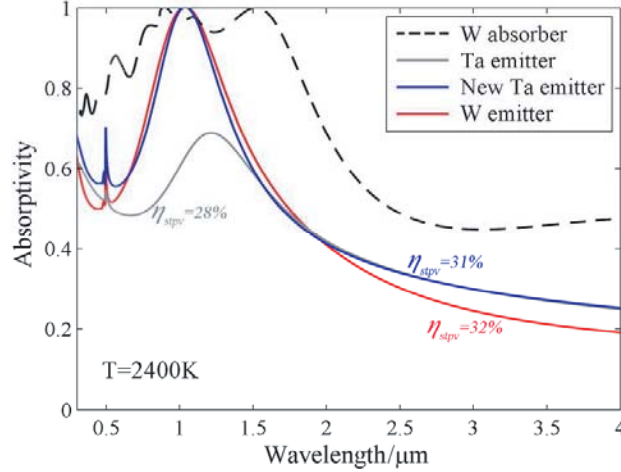
Figure 9. The calculated absorptivity of W absorber, Ta emitter, new Ta emitter ($a = 380\,\text{nm}$, $h = 150\,\text{nm}$, and $p = 500\,\text{nm}$) and W emitter ($a = 370\,\text{nm}$, $h = 160\,\text{nm}$, and $p = 500\,\text{nm}$) at temperature of 2400 K. The permittivity required for the simulation is restored by fitting the experimentally measured emittance of flat materials [27] via the Lorentz-Drude model.

system efficiencies of the two new emitters are improved (31% and 32% by our calculations). Based on the permittivity restored method, although the latest designs at high temperature did not reach our expectations (breaking the SQ limit), it did show the advantages of our proposed structures in STPV system, and it also indicated that more effort should be spent in future on the design of nanostructures using the material constants under high temperature condition to improve the whole STPV system's performance.

5. CONCLUSION

In this paper, we have proposed an all-metallic nanostructured selective absorber (W) and emitter (Ta) for STPV applications. This proposed selective absorber has approximately unity absorptance below the cutoff wavelength to maximize the absorbed solar energy, and a much lower emittance beyond the cutoff wavelength to minimize the thermal reemission. The proposed selective emitter has a sharp emittance peak at the band-gap, which can not only suppress the sub-band-gap emission, but also restrict the bandwidth of the emission above the band-gap. Both structures are polarization-independent and insensitive to the angle of incidence. We have shown through detailed balance calculation that its solar cell efficiency exceeds the Shockley-Queisser limit of 41% over a broad range of module temperatures. In addition, the structures are simple and easy to manufacture. For instance, the hexagonal close-packed triangular array structure can be achieved by self-assembly lithography, while the square array can be obtained using laser interference exposure method. The structures are made of refractory materials only and no other additional media, meaning that its performance will remain stable and reliable even at high temperatures. All these advantages give this design the potential to be employed in the actual STPV systems.

REFERENCES

1. Shockley, W. and H. J. Queisser, "Detailed balance limit of efficiency of pn junction solar cells," *Journal of Applied Physics*, Vol. 32, No. 3, 510–519, 1961.

2. De Vos, A. and H. Pauwels, "On the thermodynamic limit of photovoltaic energy conversion," *Applied Physics*, Vol. 25, No. 2, 119–125, 1981.

3. Wiemer, M., V. Sabnis, and H. Yuen, "43.5% efficient lattice matched solar cells," *Proc. SPIE*, Vol. 8108, No. 810804, 2011.

4. Swanson, R. M., "A proposed thermophotovoltaic solar energy conversion system," *Proc. IEEE*, Vol. 67, No. 3, 446–447, 1979.

5. Ruppel, W. and P. Wurfel, "Upper limit for the conversion of solar energy," *IEEE Trans. Electron. Dev.*, Vol. 27, No. 4, 877–882, 1980.

6. Spirkl, W. and H. Ries, "Solar thermophotovoltaics: An assessment," *J. Appl. Phys.*, Vol. 57, No. 9, 4409–4414, 1985.

7. Landsberg, P. T. and P. Baruch, "The thermodynamics of the conversion of radiation energy for photovoltaics," *J. Phys. Math. Gen.*, Vol. 22, No. 11, 1911–1926, 1989.

8. Chaudhuri, T. K., "A solar thermophotovoltaic converter using Pbs photovoltaic cells," *Int. J. Energy Res.*, Vol. 16, No. 6, 481–487, 1992.

9. Stone, K. W., N. S. Fatemi, and L. M. Garverick, "Operation and component testing of a solar thermophotovoltaic power system," *Photovoltaic Specialists Conference, 1996, IEEE Conference Record of the Twenty Fifth*, 1421–1424, 1996.

10. Badescu, V., "Thermodynamic theory of thermophotovoltaic solar energy conversion," *J. Appl. Phys.*, Vol. 90, No. 12, 6476–6486, 2001.

11. Tobias, I. and A. Luque, "Ideal efficiency and potential of solar thermophotonic converters under optically and thermally concentrated power flux," *IEEE Trans. Electron. Dev.*, Vol. 49, No. 11, 2024–2030, 2002.

12. Harder, N. P. and P. Wurfel, "Theoretical limits of thermophotovoltaic solar energy conversion," *Semicond. Sci. Technol.*, Vol. 18, No. 5, S151–S157, 2003.

13. Badescu, V., "Upper bounds for solar thermophotovoltaic efficiency," *Renew. Energy*, Vol. 30, No. 2, 211–225, 2005.

14. Andreev, V. M., V. P. Khvostikov, O. A. Khvostikova, A. S. Vlasov, P. Y. Gazaryan, N. A. Sadchikov, and V. D. Rumyantsev, "Solar thermophotovoltaic system with high temperature tungsten emitter," *Photovoltaic Specialists Conference, 2005, IEEE Conference Record of the Thirty-first*, 671–674, 2005.

15. Vlasov, A. S., V. P. Khvostikov, O. A. Khvostikova, P. Y. Gazaryan, S. V. Sorokina, and V. M. Andreev, "TPV systems with solar powered tungsten emitters," *AIP Conf. Proc.*, Vol. 890, 327–334, 2007.

16. Rephaeli, E. and S. Fan, "Tungsten black absorber for solar light with wide angular operation range," *Applied Physics Letters*, Vol. 92, No. 21, 211107, 2008.

17. Rinnerbauer, V., Y. X. Yeng, W. R. Chan, J. J. Senkevich, J. D. Joannopoulos, M. Soljačić, and I. Celanovic, "High-temperature stability and selective thermal emission of polycrystalline tantalum photonic crystals," *Optics Express*, Vol. 21, No. 9, 11482, 2013.

18. Celanovic, I., N. Jovanovic, and J. Kassakian, "Two-dimensional tungsten photonic crystals as selective thermal emitters," *Applied Physics Letters*, Vol. 92, No. 19, 193101, 2008.

19. Yeng, Y. X., M. Ghebrebrhan, P. Bermel, and W. R. Chan, "Enabling high-temperature nanophotonics for energy applications," *Proceedings of the National Academy of Sciences*, Vol. 109, No. 7, 2280–2285, 2012.

20. Nam, Y., Y. X. Yeng, A. Lenert, P. Bermel, I. Celanovic, M. Soljačić, and E. N. Wang, "Solar thermophotovoltaic energy conversion systems with two-dimensional tantalum photonic crystal absorbers and emitters," *Solar Energy Materials and Solar Cells*, Vol. 122, 287–296, 2014.

21. Rephaeli, E. and S. Fan, "Absorber and emitter for solar thermo-photovoltaic systems to achieve efficiency exceeding the Shockley-Queisser limit," *Optics Express*, Vol. 17, No. 17, 15145–15159, 2009.

22. Sergeant, N. P., M. Agrawal, and P. Peumans, "High performance solar-selective absorbers using coated sub-wavelength gratings," *Optics Express*, Vol. 18, No. 6, 5525–5540, 2010.

23. Lenert, A., D. M. Bierman, Y. Nam, W. R. Chan, I. Celanović, M. Soljačić, and E. N. Wang, "A nanophotonic solar thermophotovoltaic device," *Nature Nanotechnology*, Vol. 9, No. 2, 126–130, 2014.

24. Chou, J. B., Y. X. Yeng, A. Lenert, V. Rinnerbauer, I. Celanovic, M. Soljačić, E. N. Wang, and S. G. Kim, "Design of wide-angle selective absorbers/emitters with dielectric filled metallic photonic crystals for energy applications," *Optics Express*, Vol. 22, No. 101, A144–A154, 2014.

25. Mo, L., L. Yang, E. H. Lee, and S. He, "High-efficiency plasmonic metamaterial selective emitter based on an optimized spherical core-shell nanostructure for planar solar thermophotovoltaics," *Plasmonics*, Vol. 10, No. 3, 529–538, 2015.

26. Shackelford, J. F., Y. H. Han, S. Kim, and S. H. Kwon, *CRC Materials Science and Engineering Handbook* CRC Press, Florida, 2015.

27. Touloukian, Y. S. and D. P. DeWitt, *Thermophysical Properties of Matter*, The TPRC Data Series, IFI/Plenum, New York-Washington, 1970.

28. Roberts, S., "Optical properties of nickel and tungsten and their interpretation according to Drude's formula," *Physical Review*, Vol. 114, No. 1, 104, 1959.